Showcasing research from Professor Guangxue Feng's laboratory at the State Key Laboratory of Luminescent Materials and Devices, School of Materials Science and Engineering, South China University of Technology, Guangzhou, China.

A biocompatible pure organic porous nanocage for enhanced photodynamic therapy

A biocompatible pure organic porphyrin nanocage with enhanced both type I and type II ROS generation is reported for photodynamic therapy. This new strategy shall open new paradigms in developing effective photosensitizers.

As featured in:

See Yating Hu, Ruiyuan Liu, Guangxue Feng *et al.*, *Mater. Horiz.*, 2023, **10**, 4868.

ROYAL SOCIETY OF CHEMISTRY

rsc.li/materials-horizons

Registered charity number: 207890

Materials Horizons

ROYAL SOCIETY OF CHEMISTRY

COMMUNICATION

View Article Online
View Journal | View Issue

Cite this: *Mater. Horiz.*, 2023, **10**, 4868

Received 9th August 2023,
Accepted 21st September 2023

DOI: 10.1039/d3mh01263h

rsc.li/materials-horizons

A biocompatible pure organic porous nanocage for enhanced photodynamic therapy†

Zhong-Hong Zhu, ‡[a] Di Zhang,‡[a] Jian Chen, [b] Hua-Hong Zou, [c] Zhiqiang Ni,[a] Yutong Yang,[a] Yating Hu, *[d] Ruiyuan Liu, *[b] Guangxue Feng *[a] and Ben Zhong Tang[e]

Porphyrin-based photosensitizers have been widely utilized in photodynamic therapy (PDT), but they suffer from deteriorating fluorescence and reactive oxygen species (ROS) due to their close π–π stacking. Herein, a biocompatible pure organic porphyrin nanocage (Py-Cage) with enhanced both type I and type II ROS generation is reported for PDT. The porphyrin skeleton within the Py-Cage is spatially separated by four biphenyls to avoid the close π–π stacking within the nanocage. The Py-Cage showed a large cavity and high porosity with a Brunauer–Emmett–Teller surface area of over 300 $m^2 g^{-1}$, facilitating a close contact between the Py-Cage and oxygen, as well as the fast release of ROS to the surrounding microenvironment. The Py-Cage shows superb ROS generation performance over its precursors and commercial ones such as Chlorin E6 and Rose Bengal. Intriguingly, the cationic π-conjugated Py-Cage also shows promising type I ROS (superoxide and hydroxyl radicals) generation that is more promising for hypoxic tumor treatment. Both *in vitro* cell and *in vivo* animal experiments further confirm the excellent antitumor activity of the Py-Cage. As compared to conventional metal coordination approaches to improve PDT efficacy of porphyrin derivatives, the pure organic porous Py-Cage demonstrates excellent biocompatibility, which is further verified in both mice and rats. This work of an organic porous nanocage shall provide a new paradigm for the design of novel, biocompatible and effective photosensitizers for PDT.

New concepts

Porphyrin-based photosensitizers (PSs) have been widely utilized in photodynamic therapy (PDT), but suffer from deteriorating fluorescence and reactive oxygen species (ROS) generation in aggregates due to their close π–π stacking. The development of porous frameworks provides new solutions to weaken π–π stacking of porphyrin-based PSs. To the best of our knowledge, this is the first example of a pure organic nanocage that has been reported for PDT, which not only significantly improves the ROS generation and PDT performance but also avoids the biotoxicity of heavy metal ions faced by other porous materials such as metal organic frameworks (MOFs) or metallacages. The excellent biocompatibility of the Py-Cage has been successfully validated in tumor-bearing mice, healthy mice and healthy rats, through thorough analysis of blood routine parameters, blood biochemistry, and cytokine levels, as well as H & E staining.

1. Introduction

Photodynamic therapy (PDT) as a novel alternative to conventional cancer treatment approaches has attracted extensive attention recently, due to its minimal invasiveness, excellent biocompatibility and high spatiotemporal control manners.[1–3] PDT relies on photosensitizers (PSs) to photochemically react with the ground-state oxygen molecules (oxygen, $^3O_2$) or small molecules. Therefore, highly toxic reactive oxygen species (ROS) under light irradiation are generated *in situ* to induce tumor cell apoptosis or necrosis, vascular damage, cancer-mediated immunity, *etc.*[4,5] According to the different ROS generation

[a] *State Key Laboratory of Luminescent Materials and Devices, Guangdong Provincial Key Laboratory of Luminescence from Molecular Aggregates, School of Materials Science and Engineering, South China University of Technology, Guangzhou, 510640, China. E-mail: fenggx@scut.edu.cn*
[b] *Guangdong Provincial Key Laboratory of Medical Image Processing, School of Biomedical Engineering, Southern Medical University, Guangzhou, 510515, China. E-mail: ruiyliu@smu.edu.cn*
[c] *School of Chemistry and Pharmaceutical Sciences, State Key Laboratory for Chemistry and Molecular Engineering of Medicinal Resources, Guangxi Normal University, Guilin 541004, P. R. China*
[d] *Guangzhou Key Laboratory of Low-Dimensional Materials and Energy Storage Devices, School of Materials and Energy, Guangdong University of Technology, Guangzhou 510006, China. E-mail: yatinghu@gdut.edu.cn*
[e] *Shenzhen Institute of Aggregate Science and Engineering, School of Science and Engineering, The Chinese University of Hong Kong, Shenzhen 518172, China*
† Electronic supplementary information (ESI) available. See DOI: https://doi.org/10.1039/d3mh01263h
‡ Z.-H. Zhu and D. Zhang contributed equally to this work.

mechanisms and processes, PSs can be categorized into two groups: type-I and type-II PSs.[6–8] The type-I PSs involve a charge or electron transfer process from excited PSs to surrounding substances (*e.g*, water or oxygen) to catalyze the generation of highly toxic free radicals, such as superoxide ($^{\bullet}O_2^-$) or hydroxyl radicals ($^{\bullet}OH$),[9–11] while the type-II PSs rely on the efficient energy transfer from their excited triplet state to the neighboring oxygen to generate singlet oxygen species ($^1O_2$).[12,13] To date, the majority of these developed or clinically approved PSs belong to the type-II PS category. As compared to these type-II PSs, the newly emerging type-I PSs are much less oxygen-dependent and more suitable for treatment of hypoxic solid tumors, but only a few type-I PSs have been exploited until now.[14,15]

Since the first discovery of PSs based on hematoporphyrin derivatives (HpD) in 1960, the in-depth exploration of porphyrin-based PSs and their PDT performance has kicked off.[16] To date, various porphyrin-based PSs with different structures have been approved for clinical practice, such as verteporfin, porfimer sodium, temoporfin, photocarcinosin, *etc.*[17,18] Despite great progress in clinical practice, the ROS generation of these porphyrin-based PSs is still far from satisfactory. One of the main reasons is their large planar and rigid structures, which have the tendency to form tight aggregates with strong π–π stacking interactions at high concentrations in aqueous solutions or at tumor tissues.[19] Such π–π stacking results in largely diminished fluorescence and compromised ROS, leading to low PDT efficacy.[20–23] Several strategies have been applied to fight against the aggregation-caused-quenching (ACQ) effect, including modification of long amphiphilic chains, introduction of molecular spacers, and loading porphyrin PSs at nanoparticle surfaces, but with limited success.[24–27]

The development of porous frameworks provides a new solution to weaken the π–π stacking of porphyrin-based PSs.[28,29] One of the particular examples is metal–organic frameworks (MOFs) where the high porosity of MOFs can spatially separate these porphyrin molecules to avoid close π–π stacking and weaken the ACQ effect.[30–35] However, nanoscale MOFs are usually obtained by sonication or grinding, and it remains challenging to obtain MOFs with nanoscaled uniformity, excellent biocompatibility, high aqueous stability and water dispersibility.[36] Recently, discrete artificial metallacages constructed by coordination-driven self-assembly have shown natural advantages of water solubility, size and morphology control over MOFs.[37–45] Several metallacages have been reported for PDT, showing attractive prospects. For example, Sun *et al.* synthesized an octanuclear organopalladium metallacycle using a perylene-diamide ligand for fluorescence imaging and PDT.[46] Wang and Tang *et al.* constructed a prism-like metallacage using aggregation-induced emission fluorogens and $Pt(PEt_3)_2(OTf)_2$ for photodynamic and photothermal synergistic therapy.[47] Chen *et al.* developed a discrete Pt-porphyrin metallacage with improved $^1O_2$ production for PDT and chemotherapy.[48] Despite the great merits of nanoscaled MOFs and metallacages, heavy metals (*e.g.*, Zr, Hf, Pt, Zn, *etc.*) are always employed as the connection joints, which bring inherent cytotoxicity that is of significant concern in clinical applications.[28–34,38–40] Compared with metallacages, construction of pure organic nanocages based on porphyrins can effectively avoid the enrichment of heavy metals in organisms, while preserving the advantages of porous frameworks for PDT, but such a strategy has not been explored.

Herein, we report a porphyrin-based pure organic porous nanocage with enhanced type I and type II ROS generation for PDT for the first time. The pure organic nanocage (Py-Cage) is obtained by linking two 4,4′,4″,4‴-(porphyrin-5,10,15,20-tetrayl)tetrakis(*N*,*N*-dimethylaniline) (PyTtDy) molecules with four 4,4′-bis(bromomethyl)-1,1′-biphenyl ligands as the spacer (Scheme 1a). The Py-Cage shows a Brunauer–Emmett–Teller (BET) surface area of 306.4 $m^2\ g^{-1}$ with a Barrett–Joyner–Halenda (BJH) adsorption average pore width (4 V $Å^{-1}$) of 4.2 nm and two PyTtDy moieties within the nanocage have a long distance of 11.4 Å (estimated from the sum of the lengths of two phenyl rings). The long distance and large cavity effectively weaken the π–π stacking effect of porphyrins within the nanocage, and the Py-Cage exhibits excellent anti-ACQ features at high concentrations in aqueous solution. The large cavity and high porosity of the Py-Cage also promote its interactions with oxygen, leading to largely boosted ROS generation that is superb compared to its PyTtDy precursor as well as the widely used PSs including Chlorin E6 (Ce6) and Rose Bengal (RB) (Scheme 1b). Intriguingly, the pyridine cationization during Py-Cage synthesis also increases the charge separation and transfer capability, leading to the radical generation for porphyrin-based PSs for the first time (Scheme 1b). Both *in vitro* cell experiments and *in vivo* mouse tumor models further show that the Py-Cage possesses superior light-driven anti-tumor effects. In addition, several animal models including healthy mice, tumor-bearing mice, and healthy rats demonstrate the very excellent biocompatibility of the Py-Cage, as manifested by blood routine parameters, blood biochemical and cytokine parameters, H & E staining, *etc.* To the best of our knowledge, this is the first example of a porphyrin-based pure organic porous nanocage that has ever been developed for PDT, which attenuates the ACQ effect, increases oxygen interactions, produces highly toxic free radicals, and possesses excellent biocompatibility at the same time delivering a promising noninvasive PDT performance. This work provides a vivid example for the design and synthesis of novel biocompatible porous PSs and opens up new horizons for PDT-related theranostic applications.

2. Results and discussion

2.1 Synthesis and characterization of Py-Cage

To synthesize Py-Cage, PyTtDy and 4,4′-bis(bromomethyl)-1,1′-biphenyl were dissolved in excess *N*,*N*-dimethylformamide (DMF) and refluxed at 160 °C for three days, and the Py-Cage was obtained as a dark green powder (Scheme S1, ESI†). The successful synthesis of the Py-Cage was confirmed using high-resolution electrospray mass spectrometry (HRESI-MS) and Fourier transform infrared spectroscopy (FTIR). HRESI-MS shows five groups of molecular ion peaks in the range of *m*/*z* = 300–1000, with valence states ranging from +7–+3,

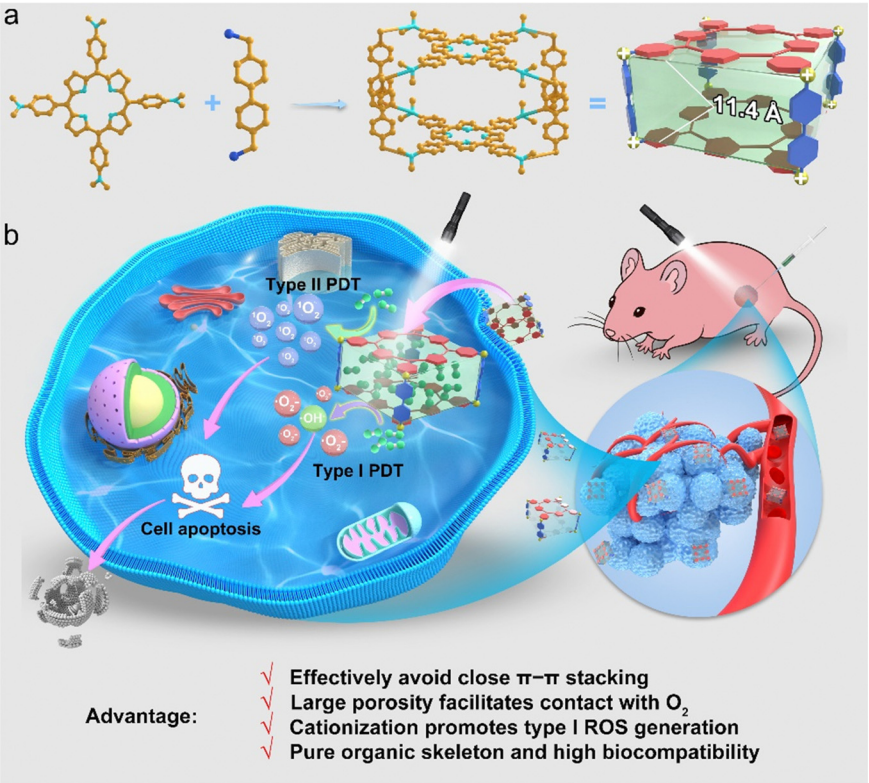

Scheme 1 (a) Schematic of the synthesis of the Py-Cage; (b) schematic of the working mechanism of the Py-Cage: the Py-Cage enhances the generation of type I ($^{\bullet}OH$ and $^{\bullet}O_2^-$) and type II ($^1O_2$) ROS under white light irradiation to induce cell apoptosis and death for PDT applications.

respectively (Fig. 1a). These molecular ion peaks with different valence states and molecular weights were attributed to cage-structured $(C_{160}H_{148}N_{16})^{8+}$ coupled with different counter anions, including $(CH_3O)^-$, $(OH)^-$, and Br^-, as shown in Fig. 1a. The experimental values of the molecular ion peaks of different valence states are in good agreement with the simulated values, confirming that the molecular formula of the obtained dark green powder is $(C_{160}H_{148}N_{16})^{8+}\cdot 8(Br^-)$. The disappeared –C–Br bond stretching vibration and bending vibration at 500–700 cm^{-1} in the FTIR absorption spectrum suggested the absence of raw material 4,4′-bis(bromomethyl)-1,1′-biphenyl in the final product (Fig. S1, ESI†). The successful synthesis of the Py-Cage was also verified by the characteristic FTIR peaks of functional groups (–NH, $–CH_3$, $–CH_2$, –C═C–, –C═N–, *etc.*) in the range of 3450–800 cm^{-1}. In addition, ^1H and ^{13}C NMR also confirmed the chemical structure of the Py-Cage (Fig. S2, ESI†). The Py-Cage showed excellent thermal stability, which did not lose any weight below 87 °C and lost three free DMF molecules (experimental value: 7.35%; theoretical value: 7.46%) in the temperature range from 87 to 300 °C. Further increasing temperature to above 380 °C leads to the decomposition of the Py-Cage with a residue of 45.16% (Fig. S3, ESI†).

The nitrogen (N_2) adsorption and desorption test of the Py-Cage at 77 K generated a BET surface area of 306.4 $m^2\ g^{-1}$ (Fig. 1b), with a BJH adsorption average pore width (4 V $Å^{-1}$) of 4.2 nm (Fig. 1c). The high specific surface area and large cavity volume suggested the successful synthesis of the porous nanocage, which could efficiently reduce porphyrin π–π stacking within the nanocage and increase its interactions with oxygen molecules, beneficial for boosting ROS production. The synthesized Py-Cage powder showed strong powder X-ray diffraction (PXRD) peaks in the 2 theta range of 8 to 32 degrees, indicating its high crystallinity (Fig. 1d). The Py-Cage also showed excellent water dispersibility, as dissolving the Py-Cage in aqueous solution (containing 1% DMSO) yielded uniformly dispersed nanoparticles with a hydrodynamic diameter of 92.6 nm as reveled by dynamic light scattering (DLS) (Fig. 1e). Transmission electron microscopy (TEM) imaging further reveals that the above porous nanoparticles are highly homogeneous and resembles the shape of petals with a size of 74.4 nm, which also suggests the porous nature of the formed nanospheres and the loose packing of the Py-Cage inside these nanospheres (Fig. 1f and Fig. S4, ESI†). High-resolution TEM (HRTEM) imaging shows that the Py-Cage has a well-defined lattice and clear electron diffraction patterns, which are consistent with the PXRD results (Fig. S4, ESI†). In addition, these nanospheres in aqueous solution well maintained their crystalline state, as revealed by the nearly unchanged PXRD spectra after dispersing the Py-Cage in aqueous solution for 48 h. Moreover, the hydrodynamic sizes (~92 nm) and polydispersity index (PDI, ~0.21) of the Py-Cage dispersed in H_2O, PBS or Dulbecco's modified Eagle's medium (DMEM) did not change significantly within 15 days of storage (Fig. S5, ESI†), indicating that the Py-Cage has high colloidal stability and is suitable for

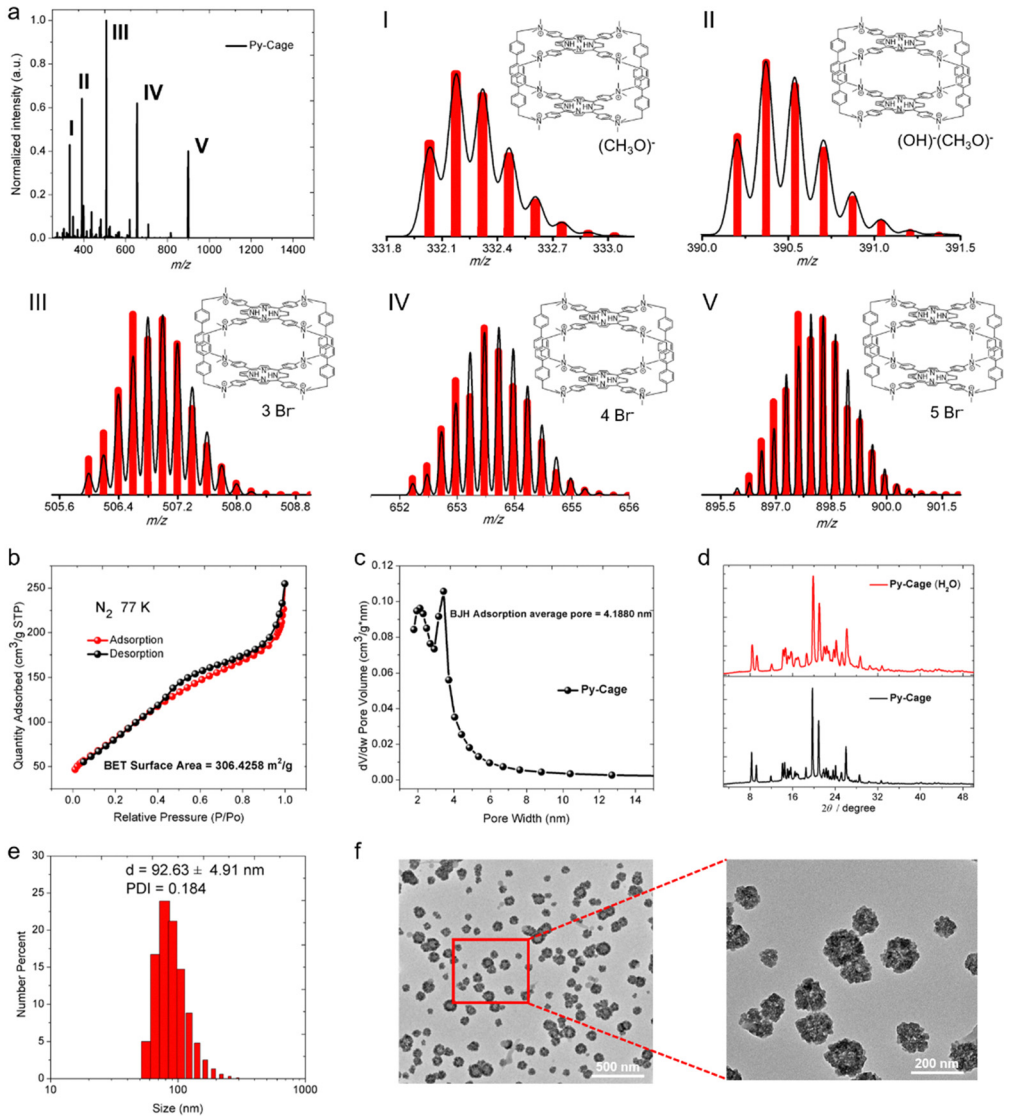

Fig. 1 (a) HRESI-MS of the Py-Cage, black is the experimental value, red is the theoretical value; (b) N_2 adsorption and desorption curves of the Py-Cage at 77 K; (c) pore size distribution of the Py-Cage obtained from adsorption experiments; (d) PXRD comparison of the Py-Cage before and after immersion in aqueous solution for 48 h; (e) particle size distribution of the Py-Cage dispersed in aqueous solution; (f) TEM of the Py-Cage dispersed in mixture solvent H_2O/DMSO (v_{water}/v_{DMSO} = 99 : 1).

use in biological applications. Collectively, these results clearly demonstrate the successful synthesis of stable and uniform porous nanoparticles from the self-assembly of these independent porous Py-Cage units.

2.2 Photophysical properties of the Py-Cage

PyTtDy and its cationic product (PyTtDy-CH_3I) were selected as the control groups for comparison (Scheme S2, ESI†).[49,50] The structure of PyTtDy-CH_3I was confirmed by HRMS, ^1H and ^{13}C NMR (Fig. S6 and S7, ESI†). Four groups of high-intensity molecular ion peaks with different valence states in the range of m/z = 200–1500 were resolved as $(C_{56}H_{62}N_8)^{4+}$ (m/z = 211.63), $(C_{56}H_{62}N_8)^{4+}\cdot(I^-)$ (m/z = 324.48), $(C_{56}H_{62}N_8)^{4+}\cdot 2(I^-)$ (m/z = 550.17) and $(C_{56}H_{62}N_8)^{4+}\cdot 3(I^-)$ (m/z = 1227.22) (Fig. S6b–e, ESI†). All three analogues showed the characteristic porphyrin absorption bands with typical Soret bands at ~420 nm and Q bands in the range of 450–670 nm in a H_2O/DMSO (v/v = 99 : 1) mixture. The Py-Cage shows distinct Q band absorption peaks at 520, 571 and 660 nm, respectively, which are much stronger than those of PyTtDy-CH_3I and PyTtDy, beneficial for light harvesting ability in the visible region (Fig. 2a).[28,31,35] For example, the Py-Cage shows a high molar absorptivity of 2.36×10^5 M^{-1} cm^{-1} (based on PyTtDy) at the Soret band of ~420 nm, which is about 15.7 and 16.9-fold higher than those of PyTtDy (1.5×10^4 M^{-1} cm^{-1}, 445 nm) and PyTtDy-CH_3I (1.4×10^4 M^{-1} cm^{-1}, 417 nm), respectively. Even though there are two PyTtDy units in one Py-Cage, its molar absorptivity is still twice larger than that of PyTtDy and the cationic product PyTtDy-CH_3I.

Both Py-Cage and PyTtDy-CH_3I showed one broad emission peak at 680 nm and 670 nm, respectively (Fig. 2b), while PyTtDy exhibited dual emission peaks at 660 nm and 690 nm, respectively.

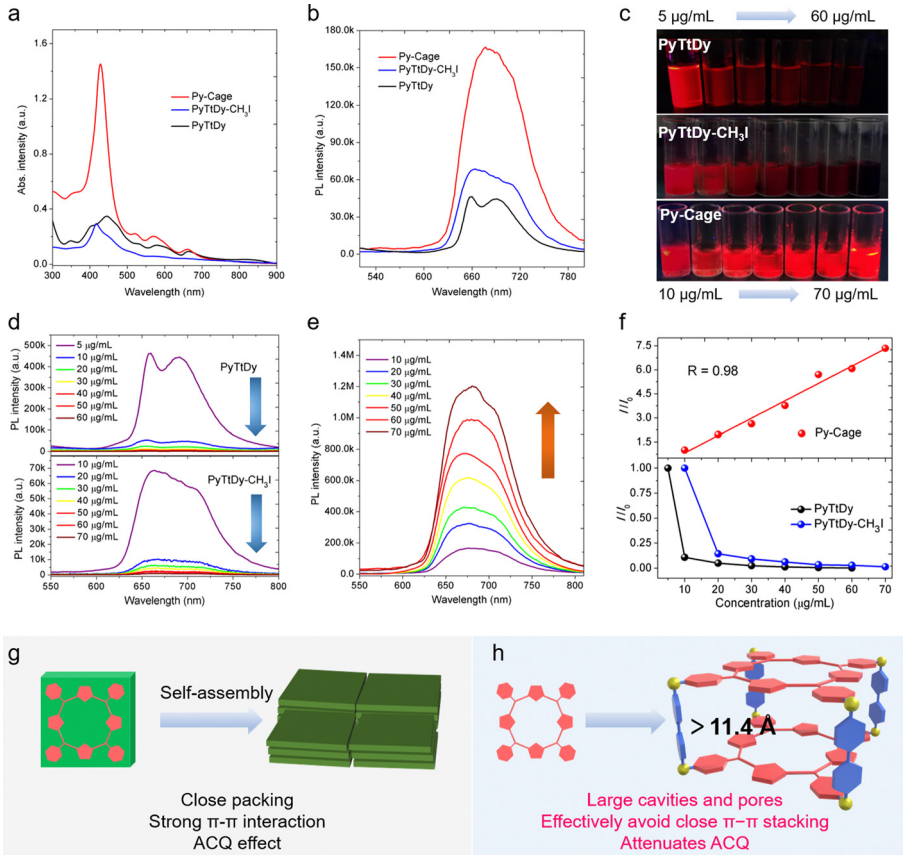

Fig. 2 UV-vis absorption spectra (a) and fluorescence (PL) spectra (b) of the Py-Cage, PyTtDy-CH_3I, and PyTtDy (10 μg mL^{-1}) in H_2O/DMSO (v_{water}/v_{DMSO} = 99 : 1) mixture solvent. (c) Photographs of the Py-Cage, PyTtDy-CH_3I, and PyTtDy in aqueous solution (1% DMSO) at different concentrations under UV light at 365 nm. Fluorescence spectra of aqueous solutions of PyTtDy (d, top), PyTtDy-CH_3I (d, bottom) and the Py-Cage (e) with different concentrations. (f) The fluorescence intensity changes of the Py-Cage, PyTtDy-CH_3I, and PyTtDy with increasing concentration. (g) and (h) Schematic comparison between traditional planar porphyrin-based photosensitizers and the porous porphyrin nanocage in attenuating the ACQ effect.

The Py-Cage at 10 μg mL^{-1} showed much stronger fluorescence brightness over PyTtDy and the cationic PyTtDy-CH_3I, hinting that the porous nanocage structure helped to reduce π–π interaction-caused fluorescence quenching. To further explore the anti-ACQ effect of the Py-Cage, its fluorescence brightness at different concentrations was investigated (Fig. 2b). Under a 365 nm UV lamp, PyTtDy showed strong red fluorescence at a low concentration of 5 μg mL^{-1}, while such fluorescence decreased significantly when increasing the PyTtDy concentration and nearly no emission could be observed even at 20 μg mL^{-1} (Fig. 2c and d). A similar phenomenon was also observed for PyTtDy-CH_3I. In sharp contrast, the Py-Cage showed gradually increased fluorescence brightness along with the increased concentrations (Fig. 2c and e). Quantitative analysis revealed an 88.9% fluorescence reduction upon increasing the PyTtDy concentration from 5 to 10 μg mL^{-1}, suggesting a typical ACQ effect. PyTtDy-CH_3I showed a slightly reduced concentration-caused quenching effect as compared to PyTtDy, which should be attributed to its increased water solubility. In the case of Py-Cage, it shows a linearly increased fluorescence intensity in the range from 10 to 70 μg mL^{-1} (Fig. 2f), hinting that concentration caused quenching is not applicable to the Py-Cage, and such a nanocage formulation can largely attenuate the ACQ effect. Porphyrin possesses a rigid and planar structure, which is normally tightly packed in aggregate and induces strong π–π interactions to quench fluorescence (Fig. 2g). Efforts to increase the water solubility only shows limited success as aggregation of such large π-conjugated planar skeletons in aqueous solution is a naturally occurring process.[31,32] In our design, the porphyrins within the porous Py-Cage are greatly separated, and the upper and lower layers of PyTtDy are spatially separated by two phenyl rings (the distance is estimated to be greater than 11.4 Å) (Fig. 2h and Fig. S8, ESI†). In addition, the quaternary ammonium salt $-N[(CH_3)_2(CH_2)]^+$, the cationic moiety of the Py-Cage together with the presence of counter anion (Br^-) should also help reduce the intermolecular π–π stacking *via* the mutual repulsion between multiple cations and between Py-Cage molecules (Fig. 1b and f).[51,52] As a consequence, the ACQ effect is significantly attenuated for the Py-Cage even at high concentrations in aqueous solution. However, upon further increasing the Py-Cage concentration, intermolecular π–π stacking may still occur between the porphyrin skeletons of nearby Py-Cages leading to reduced fluorescence. One may introduce water soluble chains to increase the water solubility and to provide steric hindrance between these cages to avoid such inter-cage π–π stacking.

2.3 ROS generation of the Py-Cage

The ROS generation capacity of the Py-Cage is subsequently evaluated under 20 mW cm^{-2} white light irradiation, with PyTtDy-CH_3I and PyTtDy as the control groups. 2′,7′-Dichlorodihydrofluorescein (DCFH), which shows largely intensified green emission (λ_{em} = 525 nm) after reaction with ROS was used as the total ROS indicator (Fig. 3a and Fig. S9, ESI†).[35,53–55] DCFH showed a fluorescence enhancement factor of 135.4 within a 150 s irradiation period in the presence of Py-Cage and light irradiation. The blank control group with only DCFH showed negligible fluorescence enhancement under the same conditions, indicating the massive ROS from the Py-Cage. The DCFH fluorescence enhancement factors for PyTtDy-CH_3I and PyTtDy were measured as 66.7 and 15.4, respectively, which were much smaller than the one for the Py-Cage. The overall ROS generation ability follows the order of Py-Cage > PyTtDy-CH_3I > PyTtDy (Fig. 3a and Fig. S9, ESI†).

To further explore the types and amounts of different ROS, more specific ROS indicators are used. 9′,10′-Anthracenediyl-bis(methylene)dimalonic acid (ABDA), which shows reduced absorbance after reaction with $^1O_2$ was firstly used to detect the generation of $^1O_2$, the type-II ROS (Fig. 3b, c and Fig. S10, ESI†), and the $^1O_2$ generation efficacy was reflected by the ABDA decomposition rate. ABDA itself is very stable under white light irradiation (20 mW cm^{-2}), with a minimal decomposition rate k = 0.008 min^{-1} while the Py-Cage rapidly degrade ABDA with a decomposition rate of k = 0.403 min^{-1}, which is much faster than those of PyTtDy-CH_3I (0.059 min^{-1}) and PyTtDy (0.034 min^{-1}) under the same conditions. A higher ABDA decomposition rate suggests a faster and more efficient $^1O_2$ generation. Hence, the $^1O_2$ generation efficacy follows the order of Py-Cage > PyTtDy-CH_3I > PyTtDy (Fig. 3c and Fig. S10, ESI†). Most importantly, the Py-Cage showed a superb $^1O_2$ generation performance over the widely used commercial PSs and its $^1O_2$ generation efficiency was about 5.5-fold and 4.2-fold higher than those of Ce6 (0.073 min^{-1}) and RB (0.095 min^{-1}), respectively (Fig. S11, ESI†). A fluorescent $^1O_2$ sensor green (SOSG) that can be rapidly converted to green emissive

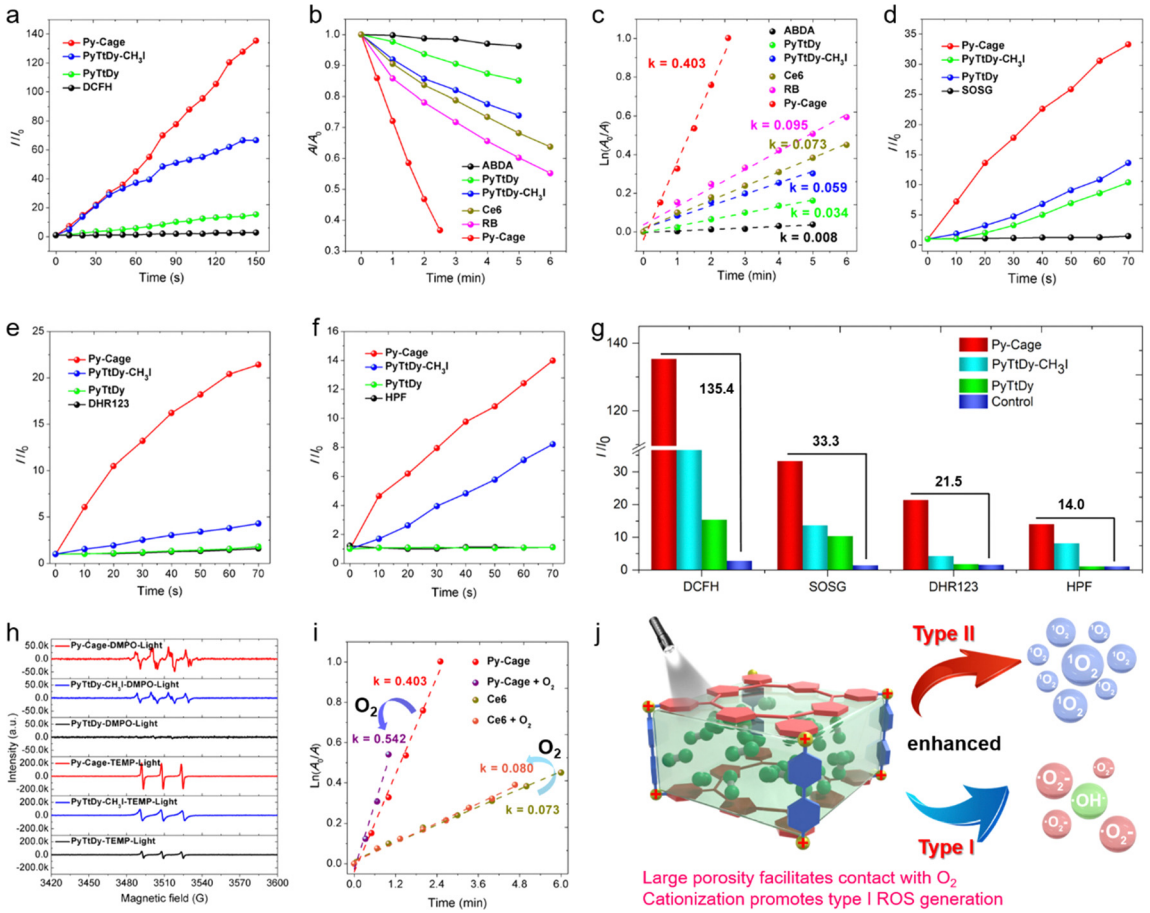

Fig. 3 (a) The ROS production of the Py-Cage, PyTtDy-CH_3I, and PyTtDy (10 μg mL^{-1}) was monitored under white light irradiation (white light, 20 mW cm^{-2}) using DCFH as an indicator, respectively, the DCFH group was the blank control group under light conditions. (b and c) The $^1O_2$ production of the Py-Cage, PyTtDy-CH_3I, PyTtDy, Ce6, and RB was monitored under white light irradiation (20 mW cm^{-2}) using ABDA as an indicator, respectively. The production of type II ($^1O_2$) and type I ($^{\bullet}O_2^-$ and $^{\bullet}OH$) ROS in the Py-Cage, PyTtDy-CH_3I, and PyTtDy was monitored under white light irradiation using SOSG (for $^1O_2$) (d), DHR123 (for $^{\bullet}O_2^-$) (e) and HPF (for $^{\bullet}OH$) (f) as indicators, respectively. (g) Comparison of different ROS generation by the Py-Cage, PyTtDy-CH_3I, and PyTtDy. (h) Comparison of the EPR results of the Py-Cage, PyTtDy-CH_3I and PyTtDy under light conditions using DMPO (DMPO-$^{\bullet}OH$ and DMPO-$^{\bullet}O_2^-$) and TEMP (TEMP-$^1O_2$) as ROS trapping agents, respectively. (i) Changes in $^1O_2$ generation for the Py-Cage and Ce6 in an oxygen environment. (j) Schematic illustration of the enhanced ROS generation for cationic organic nanocage Py-Cage.

fluorescein specifically by $^1O_2$ is also used to evaluate the $^1O_2$ generation (Fig. 3d and Fig. S12, ESI†). With a short illumination time of 70 s, the SOSG green fluorescence in the Py-Cage group increased rapidly, with an enhancement factor of 33.3, while PyTtDy-CH_3I and PyTtDy showed much smaller SOSG fluorescence enhancement factors of 13.6 and 10.4, respectively (Fig. 3g), further confirming that the Py-Cage possesses the best $^1O_2$ generation among these three PSs. Such a comparison clearly indicates that our Py-Cage is a much more powerful type-II PS that is superb over these commercial PSs, which also suggests that the construction of a porous organic nanocage is a promising strategy to improve the ROS generation of these conventional PSs.

In recent years, the development of type I PSs that generate $^{\bullet}OH$ and $^{\bullet}O_2^-$ presents a new strategy in the PDT field due to the advantage of low oxygen dependence, which show promising performance in elimination of hypoxic tumor.[9–11,14,15] This further motivates us to explore the ability of the Py-Cage to generate type I ROS. Specific free radical indicators, hydroxyphenyl fluorescein (HPF) and dihydrorhodamine 123 (DHR123), were selected for real-time monitoring of $^{\bullet}OH$ and $^{\bullet}O_2^-$ generation (Fig. 3e–g and Fig. S13, S14, ESI†). Intriguingly, within 70 s of white light illumination, the fluorescence intensity of DHR123 (25 μM) solution containing the Py-Cage (10 μg mL^{-1}) was enhanced by 21.5 times, while the enhancement factor of the PyTtDy-CH_3I group was only 4.3. Similar results were also observed for the $^{\bullet}OH^-$ probe HPF, where the HPF fluorescence intensity enhancement factors were determined to be 14.0 and 8.2 for the Py-Cage and PyTtDy-CH_3I, respectively, after 70 s illumination. It is worth noting that PyTtDy itself is not an effective type I PS as it cannot light up the fluorescence of DHR123 nor HPF under light irradiation. Considering the cationic π-conjugated nature of the Py-Cage and PyTtDy-CH_3I, it indicates that cationization engineering can efficiently improve the generation capacity of type I ROS.[53,56,57] The Py-Cage has the highest photocurrent signal and the smallest semicircle in the electrochemical impedance spectrum (EIS) among these three analogues (Fig. S15, ESI†), suggesting that the Py-Cage has the best charge separation and transport ability to undergo an electron transfer process with surrounding substrates (such as oxygen, water, *etc.*) to produce radical-type ROS. Electron paramagnetic resonance (EPR) tests were further conducted to verify the types of these generated ROS, using 2,2,6,6-tetramethyl-1-piperidine (TEMP) and 5,5-dimethyl-1-pyrroline *N*-oxide (DMPO) as ROS traps (Fig. 3h and Fig. S16, ESI†). The characteristic TEMP-$^1O_2$ peaks were observed for the Py-Cage, PyTtDy-CH_3I and PyTtDy, while the signal for the Py-Cage is much higher, revealing a higher $^1O_2$ generation ability of the Py-Cage over PyTtDy and PyTtDy-CH_3I. When using DMPO to capture free radicals, the Py-Cage yielded obvious EPR signals of DMPO-$^{\bullet}OH$ and DMPO-$^{\bullet}O_2^-$, while such signals could not be detected for PyTtDy. Although PyTtDy-CH_3I also showed obvious DMPO-$^{\bullet}OH$ peaks, the intensity was much weaker than that of the Py-Cage, further indicating the best free radical generation ability of the Py-Cage. These results further reiterated the improved ROS generation for the Py-Cage under light conditions and its newly emerging type I ROS generation capability after cationic nanocage formation.

The largely improved ROS generation for the Py-Cage should be contributed by the reduced ACQ effect and the increased oxygen contact. The greatly attenuated ACQ effect has been validated by the linearly increased fluorescence intensity along with increased concentration as shown in Fig. 2f. Concentration-dependent ROS generation was further evaluated to study the anti-ACQ effect of the Py-Cage. The commercial Ce6 with excellent water solubility is selected as the control. Ce6 only showed slightly increased ROS production upon increasing the concentration from 10 to 30 μg mL^{-1}, suggesting a notorious but unavoidable ACQ effect for planar Ce6 molecules in aqueous solution (Fig. S17–S20, ESI†). In sharp contrast, the Py-Cage showed attenuated ACQ effect as evidenced by the greatly increased ROS generation along with increased concentrations. To further prove that the hollow-cubic configuration could provide the Py-Cage more contact sites with oxygen and promote the ROS generation, an oxygen aeration experiment was further conducted. As $^1O_2$ generation is more oxygen-dependent, ABDA with high specificity towards $^1O_2$ is selected. The solution was aerated with oxygen gas for 30 min before being exposed to light irradiation and $^1O_2$ measurement (Fig. 3i and Fig. S18–S20, ESI†). In an oxygen atmosphere, the degradation rate of ABDA by the Py-Cage under light was increased to k = 0.542 min^{-1}, which was 0.139 min^{-1} higher than that in air, increased by 34.5%. In contrast, the ABDA degradation rate for Ce6 only increased from k = 0.073 to 0.080 min^{-1} upon oxygen aeration, which improved only by 0.007 min^{-1} (9.6%). The above results intuitively demonstrate the largely improved ROS generation for the Py-Cage from the aspect of interaction with surrounding oxygen. Collectively, our design of a porphyrin-based porous nanocage possesses three main features to boost the massive ROS generation as compared to conventional PSs (Fig. 3j). Firstly, the spatially separated planar porphyrin skeleton avoids the close π–π stacking within the nanocage, which greatly attenuates the ACQ effect to suppress the non-radiative decay process to increase fluorescence and excited triplet state formation. Secondly, the large cavity and high surface area provide more contact sites with surrounding oxygen to further improve the ROS generation. Thirdly, the cationic π-conjugated pyridine moieties of the Py-Cage also increase the electron separation and transfer process, affording the nanocage the capability to generate type I ROS under light that is more favorable in PDT. Moreover, such a nanocage is constructed without heavy metal as a connection joint, which is more biocompatible and avoids the side cytotoxicity associated with heavy metals.

2.4 *In vitro* PDT experiments

Encouraged by the excellent ROS generation and bright fluorescence of the Py-Cage, its PDT performance was further evaluated. Firstly, mouse breast cancer 4T1 cell was selected as the cell model to explore the cellular uptake and the photodynamic cancer cell ablation effect. The strong red fluorescence inside

cells was revealed by confocal laser scanning microscopy (CLSM) (Fig. 4a), indicating that the Py-Cage can be efficiently taken up by 4T1 cancer cells. Minimal overlap between the blue emission from the nuclei stained by DAPI and the red emission from the Py-Cage suggests that the Py-Cage is mainly located in the cytoplasm. The intracellular ROS-generating capacity of the Py-Cage was then assessed using ROS fluorescent probe 2′,7′-dichlorodihydrofluorescein diacetate (DCFH-DA), which was added to Py-Cage-incubated 4T1 cells followed by white light illumination and CLSM imaging (Fig. 4b). The bright intracellular green fluorescence from the Py-Cage group, in sharp contrast to negligible green fluorescence from the control PBS groups with or without light irradiation and the Py-Cage dark group, suggests the preferable intracellular ROS generation by the Py-Cage under light irradiation. Using dihydroethidium (DHE) to detect intracellular $^{\bullet}O_2^-$,[58,59] strong red fluorescence in the nucleus of Py-Cage-treated 4T1 cancer cells after light irradiation clearly indicates the production of intracellular $^{\bullet}O_2^-$ (Fig. S21, ESI†), while such phenomena are not observed for the control groups. These results indicate that the Py-Cage can also efficiently generate intracellular ROS including $^{\bullet}O_2^-$ after exposure to light and is promising for efficient PDT.

The PDT efficiency of the Py-Cage towards 4T1 cancer cells was explored by the standard cell counting Kit-8 (CCK-8) method and live/dead cell staining. The Py-Cage demonstrated great biocompatibility and minimal dark cytotoxicity (Fig. 4c). Under white light irradiation, the 4T1 cancer cell viability was gradually reduced in a concentration-dependent manner,

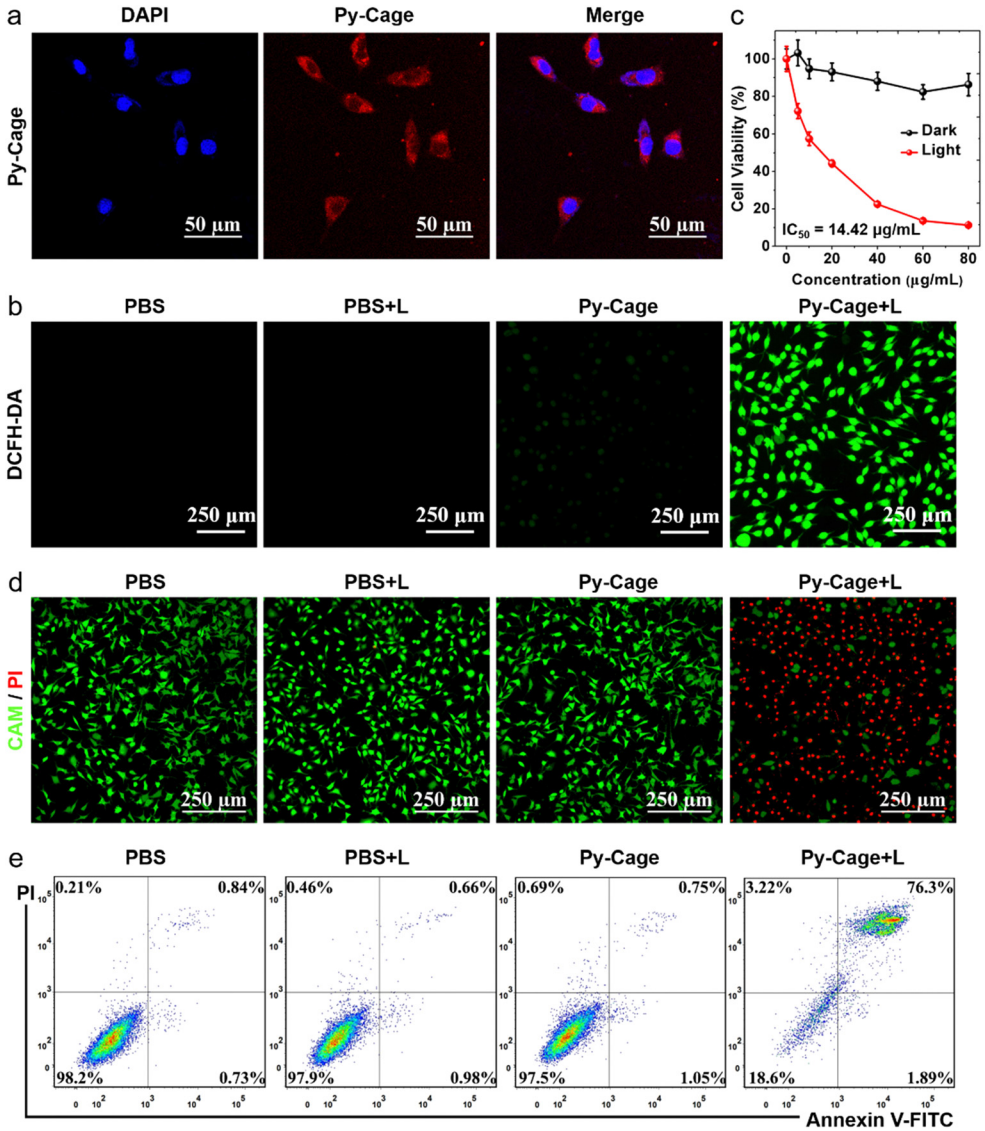

Fig. 4 (a) CLSM images of 4T1 cells after incubation with the Py-Cage (40 μg mL^{-1}) and DAPI (nucleus staining). (b) Intracellular ROS generation of the Py-Cage (40 μg mL^{-1}) inside 4T1 cells assessed by DCFH-DA probe under white light irradiation (80 mW cm^{-2}, 10 min). (c) Concentration-dependent viabilities of Py-Cage-treated 4T1 cells with or without light irradiation (80 mW cm^{-2}, 10 min) accessed by the standard CCK-8 method. Data presented mean ± standard derivation (SD), n = 3. (d) Live (CAM, green)/dead (PI, red) cell staining of Py-Cage-treated 4T1 cells. (e) Apoptosis of 4T1 cells after Py-Cage and light irradiation accessed by flow cytometric analysis.

where the cell viability was ~11.2% at a Py-Cage concentration of 80 μg mL^{-1} and the maximum half inhibitory concentration (IC_{50}) was determined to be 14.42 μg mL^{-1} (phototoxic ratio = 6.46; Fig. 4c). Next, live/dead staining with calcein AM (CAM)/propidium iodide (PI) was used to visually evaluate the killing effect on 4T1 cells (Fig. 4d and Fig. S22, ESI†). Strong green fluorescence from CAM with negligible red emission from PI was observed for PBS, PBS + L and Py-Cage groups, indicating that only light or the Py-Cage could not significantly affect the viability of the cells. In sharp contrast, the Py-Cage under light could kill nearly all the 4T1 cells as revealed by whole view of red fluorescence and the absence of green fluorescence. During the PDT process, ROS can depolarize the mitochondrial membrane and reduce the mitochondrial membrane potential and eventually leads to the release of apoptotic effectors such as cytochrome *C* (Cyt*C*), apoptosis-inducing factor (AIF), calcium ions, *etc.* to initiate apoptosis.[60,61] The apoptosis probe Annexin V-FITC was further selected to evaluate PDT performance on 4T1 cells. As shown in Fig. 4e, a large number of apoptotic cells were obviously observed in the experimental group after Py-Cage incubation and light irradiation, while cell apoptosis in the other control groups was not obvious, which further confirmed the superior anti-tumor activity of the Py-Cage under light conditions. In conclusion, the Py-Cage can generate a large amount of ROS in cells under light conditions to induce cell apoptosis and death.

2.5 *In vivo* PDT experiments and biocompatibility analysis

The PDT efficacy of the Py-Cage *in vivo* was subsequently evaluated. A 4T1 tumor bearing mouse model was constructed by subcutaneous 4T1 breast cancer cell inoculation into the right hind legs of mice. The mice were randomly divided into four groups including phosphate-buffered saline (PBS), PBS + L, Py-Cage, and Py-Cage + L groups (n = 5 mice per group). Py-Cage (300 μg mL^{-1}, 100 μL per mouse) was injected intratumorally into the selected mice when the tumor volume reached about 80 mm^3, an IVIS imaging system was used to monitor the fluorescence change. As shown in Fig. S23 (ESI†), tumors of the mice maintained a similar fluorescence signal within 4 h post injection, which still showed strong fluorescence at 48 h post injection. In this regard, PDT on mouse tumors was selected at 2 h post Py-Cage injection (irradiated at a power of 80 mW cm^{-2} for 10 min). The tumor growth curves of different groups are shown in Fig. 5a. The mice in PBS + L and Py-Cage groups showed a similar tumor growth curve to the PBS group, where tumor volumes exceeded 700 mm^3 at day 14, suggesting that only light treatment or Py-Cage treatment alone could not deliver the therapeutic effect. Remarkably, the growth of tumors in mice injected with the Py-Cage and irradiated with light was significantly inhibited, and the tumor volumes were less than 200 mm^3 within 14 days after PDT treatment (Fig. 5a). At day 14, the mice were sacrificed and the tumors were extracted and photographed. The tumors in the Py-Cage + L group showed the smallest sizes and lowest tumor weights among these groups (Fig. 5b and c), reflecting the best tumor growth inhibition performance of Py-Cage under light.

The biocompatibility of the Py-Cage was also accessed. The body weight of mice from all these four groups did not change significantly, indicating that the Py-Cage did not have obvious toxicity to mice during the treatment (Fig. 5d). Hematoxylin and

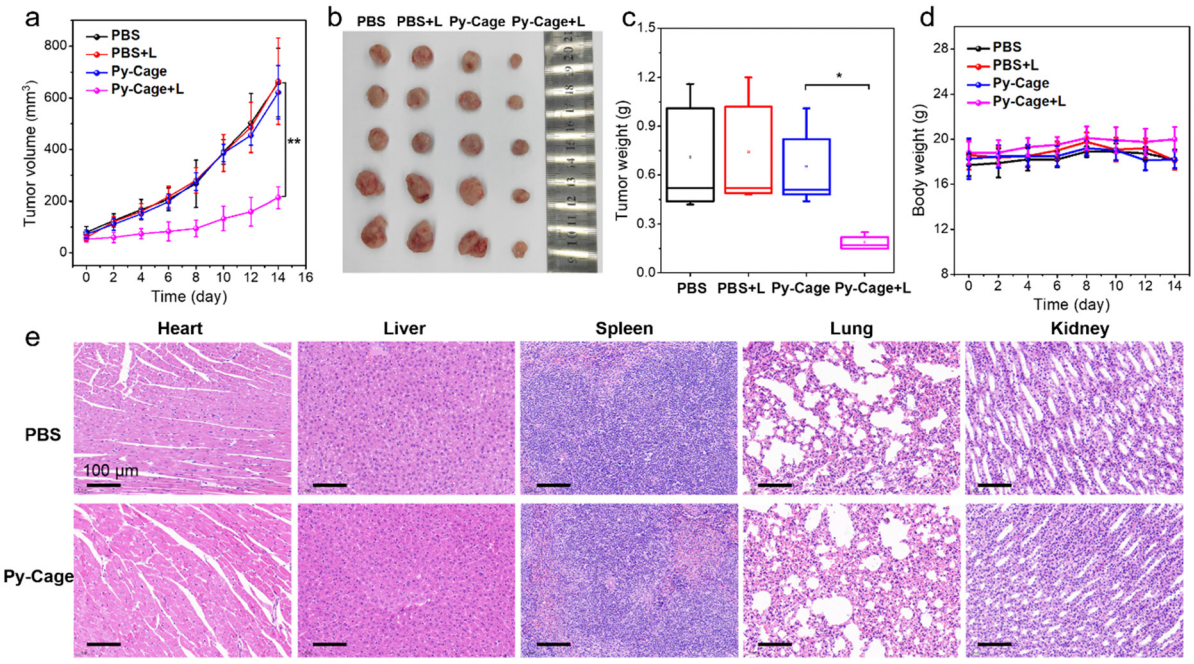

Fig. 5 (a) Tumor volume change curves of 4T1 model mice after different treatments. Tumor pictures (b) and tumor weights (c) of 4T1 tumor-bearing mice after different treatments. (d) Body weight change curves of mice in different treatment groups. (e) H & E staining of major organ sections of 4T1 tumor-bearing mice treated with PBS or Py-Cage. Data presented means ± SD. n = 5, *p < 0.05, **p < 0.01. Scale bar = 100 μm.

eosin (H & E) staining of major organs from PBS and Py-Cage groups were further accessed for the histological analysis. No obvious morphological difference is observed in the major organs (heart, liver, spleen, lung and kidney) between the Py-Cage group and the PBS control group, indicating that the Py-Cage possesses excellent biocompatibility and is suitable for *in vivo* applications (Fig. 5e). To provide more histological analysis, the Py-Cage was also intravenously injected into healthy mice through tail veins, with PBS as the control group. The body biodistribution and clearance of Py-Cage was accessed with IVIS imaging. As shown in Fig. S24 (ESI†), the Py-Cage could quickly accumulate at liver part within 2 h due to its nanoscale size, while it was effectively metabolized at 12 h post injection and *ex vivo* fluorescence images of main organs collected at 72 h post injection gave negligible fluorescence, suggesting a fast body clearance of our Py-Cage. Blood routine parameters were also analyzed at 24 h post intravenous injection of the Py-Cage or PBS into healthy mice. As shown in Fig. S25 (ESI†), the negligible changes in leukocytes related to mouse immunity such as: white blood cells (WBC and MON), lymphocytes (LYMPH), and neutrophils (GRAN) suggested that the Py-Cage will not elicit the mice infection. The parameters of red blood cells including red blood cells (RBC), hematocrit (HCT), hemoglobin (HGB), mean muscle tone (MCV), erythrocyte hemoglobin content (MCH), and erythrocyte distribution width (RDW) in the mice treated with Py-Cage did not change significantly, indicating that the mice did not develop symptoms of anemia. Platelet volume (MPV) and platelet volume distribution width (PDW) analysis showed that the Py-Cage did not cause bleeding symptoms in mice. H & E staining of main organs (collected at 72 h post injection) from the Py-Cage administered healthy mice showed healthy and normal

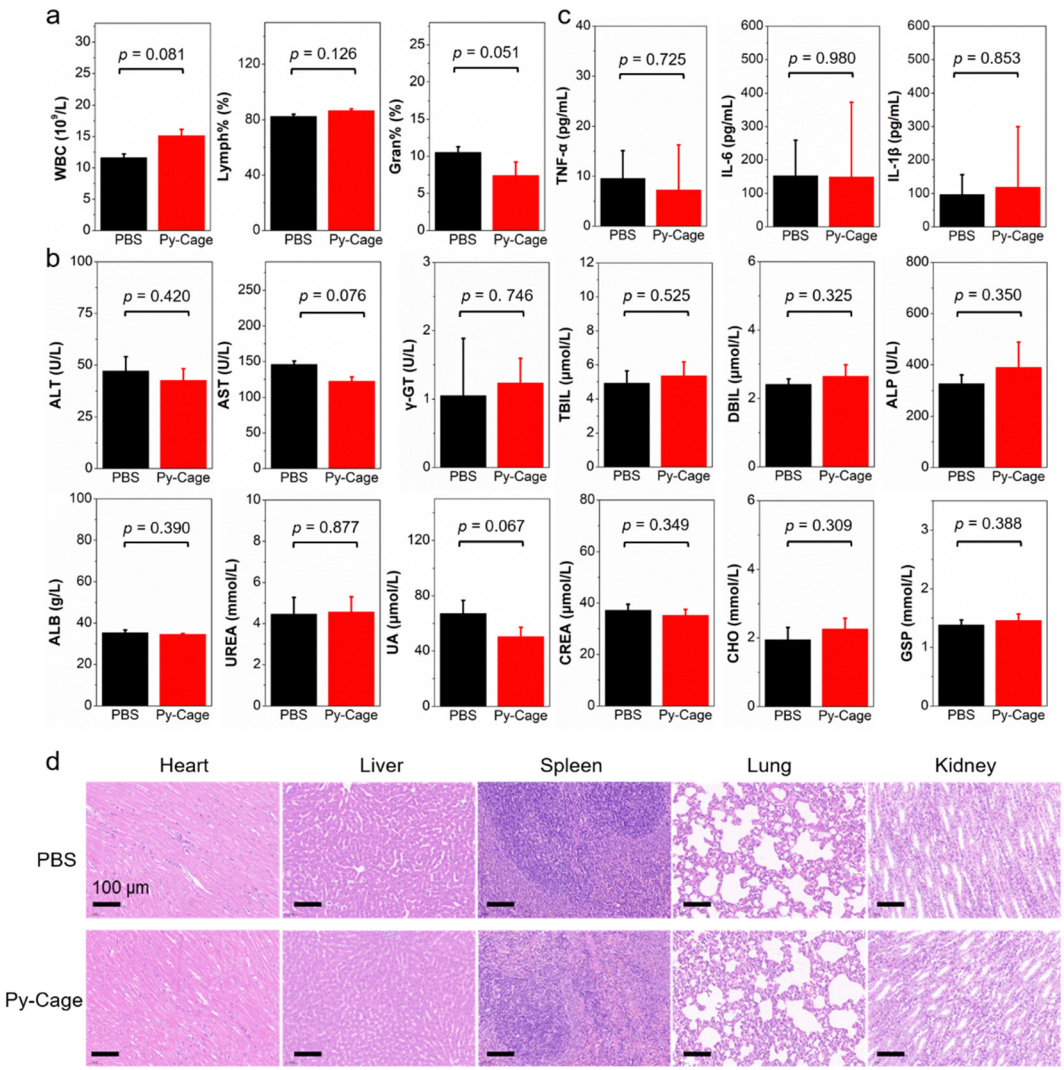

Fig. 6 Toxicological tests of the Py-Cage in healthy rats. (a) Blood routines (such as white blood cells (WBC), lymphocytes (Lymph%), and neutrophils (Gran%)); (b) blood biochemistry (alanine aminotransferase (ALT), aspartate aminotransferase (AST), γ-glutamyl transpeptidase (γ-GT), total bilirubin (TBIL), direct bilirubin (DBIL), alkaline phosphatase (ALP), albumin (ALB)) and kidney function (urea nitrogen (UREA), uric acid (UA), creatinine (CREA), *etc.*; (c) cytokines (interleukin-6 (IL-6), interleukin-1β (IL-1β) and tumor necrosis factor (TNF-α)); and (d) H & E staining images of major organ sections. Scale bar = 100 μm. Data presented means ± SD, n = 3, no significant difference.

morphologies, with minimal difference as compared to the PBS group, further indicating the excellent biocompatibility of the Py-Cage (Fig. S26, ESI†).

In addition, healthy rats were further used to study the biocompatibility of the Py-Cage, where the Py-Cage was intravenously injected into rats through the tail veins (Fig. 6 and Fig. S27, S28, ESI†). The blood routine and biochemical parameters of the rats were analyzed at 48 h post injection. As shown in Fig. 6a and Fig. S27 (ESI†), the Py-Cage does not cause infection (WBC, lymphocyte percentage (Lymph%), percentage of neutrophils (Gran%)), anemia (RBC, HCT, MCV, and RDW), or bleeding symptoms (HGB, MCH, MPV, and PDW) in rats. As shown in Fig. 6b and Fig. S28 (ESI†), there was no damage to liver function (alanine aminotransferase (ALT), aspartate aminotransferase (AST), γ-glutamyl transpeptidase (γ-GT), total bilirubin (TBIL), direct bilirubin (DBIL), alkaline phosphatase (ALP), and albumin (ALB)) and kidney function (urea nitrogen (UREA), uric acid (UA), and creatinine (CREA)) in rats after tail vein injection of Py-Cage. In addition, cholesterol (CHO), triglyceride (TG), high-density lipoprotein cholesterol (HDL), low-density lipoprotein (LDL), glucose (GLU), and glycated serum protein (GSP) levels of rats were not affected by the Py-Cage (Fig. S28, ESI†), indicating that the blood ester and sugar contents of Py-Cage-treated rats were normal. The cytokines like interleukin-6 (IL-6), interleukin-1β (IL-1β) and tumor necrosis factor (TNF-α) in rat serum were also detected, which exhibited minimal difference compared to the PBS control group, indicating that the Py-Cage will not cause inflammation or infection in the rats (Fig. 6c). Finally, H & E staining of the main organs (heart, liver, spleen, lung, and kidney) of the Py-Cage group and PBS control group showed no significant morphological difference (Fig. 6d), further indicating that the Py-Cage had excellent biocompatibility.

2.6 *In vitro* and *in vivo* PDT experiments with Py-Cage NPs

To further evaluate the potential of the Py-Cage for PDT, we also encapsulated the Py-Cage with a biocompatible block copolymer 1,2-distearoyl-*sn*-glycero-3-phosphoethanolamine-*N*-[methoxy(polyethylene glycol)-2000] (DSPE-PEG_{2000}) by a nano-precipitation method (see the Experimental section of the ESI,† Fig. 7a) to further improve its water disability and biocompatibility.[62,63] The polymer encapsulated Py-Cage nanoparticles (NPs) showed a hydrodynamic diameter of 131.3 nm and a PDI of 0.301 (Fig. 7b). TEM images suggested that the Py-Cage NPs were of

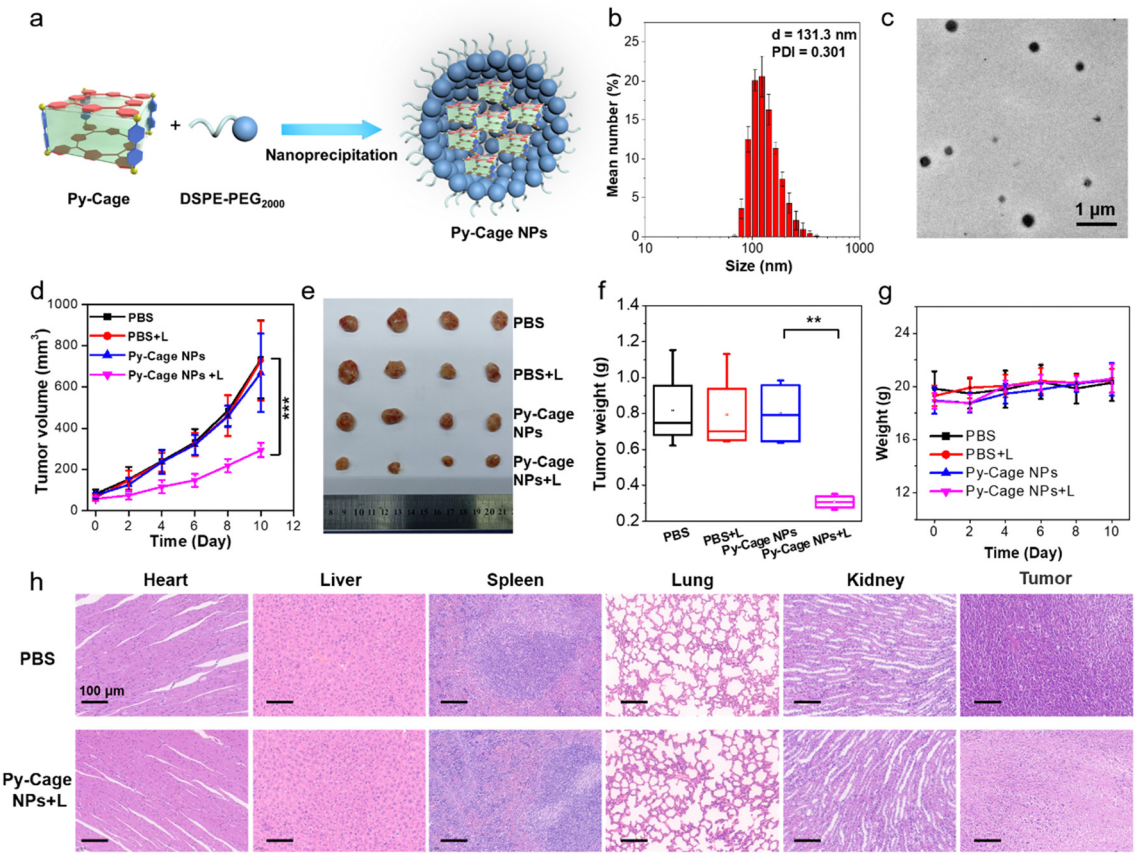

Fig. 7 (a) Schematic of Py-Cage NPs synthesized by a nanoprecipitation method with DSPE-PEG_{2000} as the encapsulation matrix. (b) Particle size distribution of Py-Cage NPs. Data presented mean ± SD, n = 3. (c) TEM image of Py-Cage NPs, Scale bar = 1 μm. Tumor volume change curves (d), tumor pictures (e), tumor weights (f), and body weight change curves (g) of 4T1 tumor-bearing mice in different groups. (h) H & E staining images of major organs and tumor sections of 4T1 tumor-bearing mice treated with PBS or Py-Cage NPs + L. Scale bar = 100 μm. Data presented means ± SD. n = 4, *p < 0.05, **p < 0.01, **p < 0.001.

spherical shape with sizes around 104.4 nm (Fig. 7c and Fig. S29a, S29b, ESI†). Py-Cage NPs at 10 μg mL^{-1} showed similar UV-Vis absorption spectrum to Py-Cage (Fig. S29c, ESI†). However, Py-Cage NPs showed a weaker PL intensity than that of the Py-Cage, which should be caused by potential intermolecular π–π stacking between Py-Cages inside the compact intraparticle microenvironment (Fig. S29d, ESI†). Different ROS indicators including DCFH, ABDA, DHR123 and HPF were further used to evaluate their ROS generation ability under white light irradiation (20 mW cm^{-2}). Py-Cage NPs showed a moderately decreased ROS generating ability as compared to the Py-Cage (Fig. S30, ESI†), which shall also be caused by the increased intermolecular π–π stacking between nearby Py-Cages inside these compact nanoparticles, while the insertion of the DSPE segment into the porous space of the Py-Cage may also reduce the oxygen interaction and hence weaken the ROS generation.

The PDT efficiency of Py-Cage NPs towards 4T1 cancer cells was explored by the standard CCK-8 method and live/dead cell staining. Py-Cage NPs demonstrated excellent biocompatibility and minimal dark cytotoxicity (Fig. S31a, ESI†). Under white light irradiation, the 4T1 cancer cell viability was gradually reduced in a concentration-dependent manner, where the cell viability was ~22.0% at a Py-Cage NP concentration of 120 μg mL^{-1} and the IC_{50} value was determined to be 37.58 μg mL^{-1} (Fig. S31b, ESI†). Live/dead staining with CAM/PI was then used to visually evaluate the killing effect of Py-Cage NPs on 4T1 cells (Fig. S32, ESI†). Strong green fluorescence from CAM with negligible red emission from PI was observed for PBS, PBS + L and Py-Cage NP (120 μg mL^{-1}) groups, indicating that only light or Py-Cage NPs could not significantly affect the viability of the cells. In sharp contrast, Py-Cage NPs (120 μg mL^{-1}) under light could kill nearly all the 4T1 cells as revealed by whole view of red fluorescence and the absence of green fluorescence. Although Py-Cage NPs also showed good cell killing ability under light irradiation, the IC_{50} value was significantly higher than that of the Py-Cage. This is mainly due to the reduced ROS generation caused by the intermolecular π–π stacking between nearby Py-Cage molecules inside Py-Cage NPs. One may introduce water-soluble chains to increase the water solubility and to provide steric hindrance between these cages to avoid such inter-cage π–π stacking. Nevertheless, in our current work, the intramolecular π–π stacking between porphyrin skeletons within one Py-Cage has been sufficiently avoided to reduce the ACQ effect. In addition, the large cavity of the Py-Cage could also increase the loading and interaction of oxygen, which is also beneficial for ROS generation and final PDT performance and our Py-Cage design shall still present an efficient strategy for designing photosensitizers for enhanced PDT.

The PDT efficacy of Py-Cage NPs *in vivo* was further studied. A 4T1 tumor bearing mouse model was established by subcutaneously inoculating 4T1 breast cancer cells into the right hind legs of nude mice. When the tumor volume reaches approximately 80 mm^3, the mice were randomly divided into four groups including PBS, PBS + L, Py-Cage NPs, and Py-Cage NPs + L groups (n = 4). Py-Cage NPs (300 μg mL^{-1}, 100 μL per mouse) were injected into the mouse bodies through the tail veins. *In vivo* fluorescence images suggested that Py-Cage NPs could quickly accumulate at tumor sites, which reached the maximum at 6 h post injection (Fig. S33, ESI†). The *ex vivo* images obtained at 8 h post injection confirmed the excellent tumor accumulation ability of Py-Cage NPs (Fig. S33, ESI†). Therefore, we performed light treatment (irradiation at a power of 80 mW cm^{-2} for 10 min) at 6 h post injection. The tumor growth curves of different groups are shown in Fig. 7d. As shown, the tumor growth of mice injected with Py-Cage NPs and irradiated with light was significantly inhibited compared to the other three groups (PBS, PBS + L, Py-Cage NPs), proving the PDT antitumor effect of Py-Cage NPs. The lack of significant weight loss in mice during the whole progress proved that Py-Cage NPs has minimal side effects (Fig. 7e). At day 10 post injection, the mice were euthanized and the tumors were extracted (Fig. 7f). The tumors from the PBS, PBS + L, and Py-Cage NPs groups showed similar weights of 0.82 g, while tumors from the Py-Cage NPs + L group were weighed to be around 0.31 g, proving the excellent anti-tumor PDT performance of Py-Cage NPs (Fig. 7f and g). H & E staining was performed on the extracted organs and tumor tissues and the results showed that the mouse organs treated with Py-Cage NPs + L did not show significant inflammation or damage, while the nuclei of tumor cells in the tumor tissue showed significant rupture and damage, further proving the excellent biocompatibility and PDT efficacy of Py-Cage NPs (Fig. 7h).

3. Conclusions

The compact π–π stacking driven by self-assembly in aqueous solution has become a major bottleneck for the application of photosensitizers with large planar and rigid structures for PDT. Although a variety of strategies have been found to weaken the self-aggregation of porphyrin-based photosensitizers in aqueous solution and the high quenching of ROS, the results are still unsatisfactory. Herein, a novel porphyrin-based porous organic nanocage (Py-Cage) was synthesized with a large cavity volume to promote both type-I and type-II ROS generation. The formation of cationic Py-Cage spatially separates the porphyrin PS within the nanocage with a distance over 11 Å (estimated from the distance of two phenyl rings). The long distance and void spaces effectively weaken the π–π stacking effect of porphyrin moieties within the nanocage, and the Py-Cage exhibits excellent anti-ACQ features to maintain bright fluorescence and ROS generation even at high concentrations in aqueous solution. In addition, the Py-Cage exhibited a very large cavity volume with a surface area of 306.4 m^2 g^{-1} and a BJH pore width of 4.2 nm. The unique porous skeleton increases its interaction with surrounding oxygens and other substrates to fully utilize the excited triplet state for ROS generation. Intriguingly, the cationic nanocage shows a pronounced charge separation and transport ability, which converted a typical type-II PS to a predominate type-I PS with remarkable free radical generation, including $^{\bullet}O_2^-$ and $^{\bullet}OH^-$. All these works cooperatively made the Py-Cage a powerful PS. Both *in vitro* cell

experiments and *in vivo* mouse experiments confirmed its excellent PDT performance. The design of Py-Cage with a pure organic porous skeleton could fully utilize the excited triplet state of PSs to generate ROS, by reducing the π–π stacking, increasing oxygen interactions and promoting charge transfer processes. In addition, the Py-Cage has also demonstrated excellent biocompatibility and biosafety in both rats and mice according to the analysis of H & E staining, blood routine parameters, blood biochemistry, and cytokine levels. Collectively, the Py-Cage provides a vivid example for enhancing the fluorescence and ROS yields of traditional porphyrin-based PSs as well as other PSs with rigid and large planar structures, which shall pave a new path for designing novel and effective PSs with excellent biocompatibility for PDT and related phototheranostic applications.

Conflicts of interest

There are no conflicts to declare.

Acknowledgements

This work was supported by the Natural Science Foundation of China (22205067), Natural Science Foundation of Guangdong Province (2021A1515011901), and Guangdong Provincial Key Laboratory of Luminescence from Molecular Aggregates (2019B030301003).

Notes and references

1 P. Agostinis, K. Berg, K. A. Cengel, T. H. Foster, A. W. Girotti, S. O. Gollnick, S. M. Hahn, M. R. Hamblin, A. Juzeniene, D. Kessel, M. Korbelik, J. Moan, P. Mroz, D. Nowis, J. Piette, B. C. Wilson and J. Golab, *CA. Cancer J. Clin.*, 2011, **61**, 250–281.
2 T. C. Pham, V.-N. Nguyen, Y. Choi, S. Lee and J. Yoon, *Chem. Rev.*, 2021, **121**, 13454–13619.
3 X. Li, J. F. Lovell, J. Yoon and X. Chen, *Nat. Rev. Clin. Oncol.*, 2020, **17**, 657–674.
4 Z. Zhou, J. Song, L. Nie and X. Chen, *Chem. Soc. Rev.*, 2016, **45**, 6597–6626.
5 L. Huang, S. Zhao, J. Wu, L. Yu, N. Singh, K. Yang, M. Lan, P. Wang and J. S. Kim, *Coord. Chem. Rev.*, 2021, **438**, 213888.
6 X. Zhao, J. Liu, J. Fan, H. Chao and X. Peng, *Chem. Soc. Rev.*, 2021, **50**, 4185–4219.
7 L. K. McKenzie, H. E. Bryant and J. A. Weinstein, *Coord. Chem. Rev.*, 2019, **379**, 2–29.
8 T. Luo, K. Ni, A. Culbert, G. Lan, Z. Li, X. Jiang, M. Kaufmann and W. Lin, *J. Am. Chem. Soc.*, 2020, **142**, 7334–7339.
9 Y.-Y. Wang, Y.-C. Liu, H. Sun and D.-S. Guo, *Coord. Chem. Rev.*, 2019, **395**, 46–62.
10 X. Li, D. Lee, J.-D. Huang and J. Yoon, *Angew. Chem., Int. Ed.*, 2018, **57**, 9885–9890.
11 Y. Zhu, Q. Wu, C. Chen, G. Yang, H. Cao, Y. Gao, L. Jiao, E. Hao and W. Zhang, *Sci. China Mater.*, 2021, **64**, 3101–3113.
12 M. Tavakkoli Yaraki, B. Liu and Y. N. Tan, *Nano-Micro Lett.*, 2022, **14**, 123.
13 W. Fan, P. Huang and X. Chen, *Chem. Soc. Rev.*, 2016, **45**, 6488–6519.
14 Y. Wan, L. Fu, C. Li, J. Lin and P. Huang, *Adv. Mater.*, 2021, **33**, 2103978.
15 D. Chen, Q. Xu, W. Wang, J. Shao, W. Huang and X. Dong, *Small*, 2021, **17**, 2006742.
16 R. L. Lipson and E. J. Baldes, *Arch. Dermatol.*, 1960, **82**, 508–516.
17 M. Ethirajan, Y. Chen, P. Joshi and R. K. Pandey, *Chem. Soc. Rev.*, 2011, **40**, 340–362.
18 J. Tian, B. Huang, M. H. Nawaz and W. Zhang, *Coord. Chem. Rev.*, 2020, **420**, 213410.
19 L. E. Bennett, K. P. Ghiggino and R. W. Henderson, *J. Photochem. Photobiol. B Biol.*, 1989, **3**, 81–89.
20 S. Singh, A. Aggarwal, N. V. S. D. K. Bhupathiraju, G. Arianna, K. Tiwari and C. M. Drain, *Chem. Rev.*, 2015, **115**, 10261–10306.
21 G. Feng and B. Liu, *Acc. Chem. Res.*, 2018, **51**, 1404–1414.
22 X. Li, C. Kim, S. Lee, D. Lee, H.-M. Chung, G. Kim, S.-H. Heo, C. Kim, K.-S. Hong and J. Yoon, *J. Am. Chem. Soc.*, 2017, **139**, 10880–10886.
23 K. M. Harmatys, J. Chen, D. M. Charron, C. M. MacLaughlin and G. Zheng, *Angew. Chem., Int. Ed.*, 2018, **130**, 8257–8261.
24 G. Feng, G.-Q. Zhang and D. Ding, *Chem. Soc. Rev.*, 2020, **49**, 8179–8234.
25 T. Luo, G. T. Nash, Z. Xu, X. Jiang, J. Liu and W. Lin, *J. Am. Chem. Soc.*, 2021, **143**, 13519–13524.
26 X. Liang, M. Chen, P. Bhattarai, S. Hameed and Z. Dai, *ACS Nano*, 2020, **14**, 13569–13583.
27 D. Shang, Q. Yu, W. Liu, S. Zhang, Y. Li, J. Chen, Z. Zhang and X. Lu, *Sci. China Mater.*, 2022, **65**, 527–535.
28 C. He, D. Liu and W. Lin, *Chem. Rev.*, 2015, **115**, 11079–11108.
29 Q. Zheng, X. Liu, Y. Zheng, K. W. K. Yeung, Z. Cui, Y. Liang, Z. Li, S. Zhu, X. Wang and S. Wu, *Chem. Soc. Rev.*, 2021, **50**, 5086–5125.
30 J. Chen, Y. Zhu and S. Kaskel, *Angew. Chem., Int. Ed.*, 2021, **60**, 5010–5035.
31 G. Lan, K. Ni and W. Lin, *Coord. Chem. Rev.*, 2019, **379**, 65–81.
32 K. Lu, T. Aung, N. Guo, R. Weichselbaum and W. Lin, *Adv. Mater.*, 2018, **30**, 1707634.
33 M. Lismont, L. Dreesen and S. Wuttke, *Adv. Funct. Mater.*, 2017, **27**, 1606314.
34 J. Hynek, M. K. Chahal, D. T. Payne, J. Labuta and J. P. Hill, *Coord. Chem. Rev.*, 2020, **425**, 213541.
35 Z.-H. Zhu, Y. Liu, C. Song, Y. Hu, G. Feng and B. Z. Tang, *ACS Nano*, 2022, **16**, 1346–1357.
36 K. A. S. Usman, J. W. Maina, S. Seyedin, M. T. Conato, L. M. Payawan, L. F. Dumée and J. M. Razal, *NPG Asia Mater.*, 2020, **12**, 58.

37 T. Hasell and A. I. Cooper, *Nat. Rev. Mater.*, 2016, **1**, 16053.
38 Y. Sun, C. Chen, J. Liu and P. J. Stang, *Chem. Soc. Rev.*, 2020, **49**, 3889–3919.
39 T. R. Cook and P. J. Stang, *Chem. Rev.*, 2015, **115**, 7001–7045.
40 A. J. McConnell, *Chem. Soc. Rev.*, 2022, **51**, 2957–2971.
41 Y. Li, Y. Dong, L. Cheng, C. Qin, H. Nian, H. Zhang, Y. Yu and L. Cao, *J. Am. Chem. Soc.*, 2019, **141**, 8412–8415.
42 H. Nian, L. Cheng, L. Wang, H. Zhang, P. Wang, Y. Li and L. Cao, *Angew. Chem., Int. Ed.*, 2021, **60**, 15354–15358.
43 H. Liu, Z. Zhang, C. Mu, L. Ma, H. Yuan, S. Ling, H. Wang, X. Li and M. Zhang, *Angew. Chem., Int. Ed.*, 2022, **61**, e202207289.
44 C. Mu, Z. Zhang, Y. Hou, H. Liu, L. Ma, X. Li, S. Ling, G. He and M. Zhang, *Angew. Chem., Int. Ed.*, 2021, **60**, 12293–12297.
45 H. Duan, Y. Li, Q. Li, P. Wang, X. Liu, L. Cheng, Y. Yu and L. Cao, *Angew. Chem., Int. Ed.*, 2020, **59**, 10101–10110.
46 L. He, L.-X. Cai, M.-H. Li, G.-L. Zhang, L.-P. Zhou, T. Chen, M.-J. Lin and Q.-F. Sun, *Chem. Sci.*, 2020, **11**, 7940–7949.
47 Y. Qin, X. Chen, Y. Gui, H. Wang, B. Z. Tang and D. Wang, *J. Am. Chem. Soc.*, 2022, **144**, 12825–12833.
48 G. Yu, S. Yu, M. L. Saha, J. Zhou, T. R. Cook, B. C. Yung, J. Chen, Z. Mao, F. Zhang, Z. Zhou, Y. Liu, L. Shao, S. Wang, C. Gao, F. Huang, P. J. Stang and X. Chen, *Nat. Commun.*, 2018, **9**, 4335.
49 H. Hu, H. Wang, Y. Yang, J. Xu and X. Zhang, *Angew. Chem., Int. Ed.*, 2022, **61**, e202200799.
50 F. Sadegh, O. Bagheri, M. Moghadam, V. Mirkhani, S. Tangestaninejad and I. Mohammadpoor-Baltork, *J. Organomet. Chem.*, 2014, **759**, 46–57.
51 L. Feng, *et al.*, *Nat. Commun.*, 2022, **13**, 1389.
52 G. Gong, *et al.*, *Angew. Chem., Int. Ed.*, 2021, **60**, 14831–14835.
53 Y. Yu, S. Wu, L. Zhang, S. Xu, C. Dai, S. Gan, G. Xie, G. Feng and B. Z. Tang, *Biomaterials*, 2022, **280**, 121255.
54 Z. Zhuang, Z. Meng, J. Li, P. Shen, J. Dai, X. Lou, F. Xia, B. Z. Tang and Z. Zhao, *ACS Nano*, 2022, **16**, 11912–11930.
55 P. Xiao, Z. Shen, D. Wang, Y. Pan, Y. Li, J. Gong, L. Wang, D. Wang and B. Z. Tang, *Adv. Sci.*, 2022, **9**, 2104079.
56 D. Barman, K. Narang, R. Parui, N. Zehra, M. N. Khatun, L. R. Adil and P. K. Iyer, *Aggregate*, 2022, **3**, e172.
57 Y. Hu, S. Yin, W. Liu, Z. Li, Y. Chen and J. Li, *Aggregate*, 2023, **4**, e256.
58 P. M. Callop, M. A. Paz, E. Henson and S. A. Latt, *Biotechniques*, 1984, **2**, 32–36.
59 S. Walrand, S. Valeix, C. Rodriguez, P. Ligot, J. Chassagne and M.-P. Vasson, *Clin. Chim. Acta*, 2003, **331**, 103–110.
60 J. C. Goldstein, N. J. Waterhouse, P. Juin, G. I. Evan and D. R. Green, *Nat. Cell Biol.*, 2000, **2**, 156–162.
61 C. B. Thompson, *Science*, 1995, **267**, 1456–1462.
62 S. Gan, W. Wu, G. Feng, Z. Wang, B. Liu and B. Z. Tang, *Small*, 2022, **18**(26), 2202242.
63 P. Cen, J. Huang, C. Jin, J. Wang, Y. Wei, H. Zhang and M. Tian, *Aggregate*, 2023, DOI: **10.1002/agt2.352**.